Coulomb gas transitions in three-dimensional classical dimer models

Gang Chen

Department of Physics, University of California, Santa Barbara, California 93106, USA

Jan Gukelberger

Department of Physics, University of California, Santa Barbara, California 93106, USA
and Microsoft Research, Station Q, University of California, Santa Barbara, California 93106, USA

Simon Trebst

Microsoft Research, Station Q, University of California, Santa Barbara, California 93106, USA

Fabien Alet

Laboratoire de Physique Théorique, Université de Toulouse, UPS, (IRSAMC), 31062 Toulouse, France
and CNRS, LPT (IRSAMC), 31062 Toulouse, France

Leon Balents

Kavli Institute for Theoretical Physics, University of California, Santa Barbara, California 93106, USA
(Received 25 March 2009; published 16 July 2009)

Close-packed, classical dimer models on three-dimensional, bipartite lattices harbor a Coulomb phase with power-law correlations at infinite temperature. Here, we discuss the nature of the thermal phase transition out of this Coulomb phase for a variety of dimer models which energetically favor crystalline dimer states with columnar ordering. For a family of these models, we find a direct thermal transition from the Coulomb phase to the dimer crystal. While some systems exhibit (strong) first-order transitions in correspondence with the Landau-Ginzburg-Wilson paradigm, we also find clear numerical evidence for continuous transitions. A second family of models undergoes two consecutive thermal transitions with an intermediate paramagnetic phase separating the Coulomb phase from the dimer crystal. We can describe all of these phase transitions in one unifying framework of candidate field theories with two complex Ginzburg-Landau fields coupled to a $U(1)$ gauge field. We derive the symmetry-mandated Ginzburg-Landau actions in these field variables for the various dimer models and discuss implications for their respective phase transitions.

I. INTRODUCTION

Constraints are a pervasive feature of strongly correlated systems. For instance, in Mott insulators, a large atomic Coulomb repulsion effectively constrains the charge of each ion to be fixed, while still allowing spin and orbital fluctuations. This situation, in which the dominant terms in the Hamiltonian impose constraints, but local fluctuations remain strong, provides a challenge to physical understanding. In frustrated magnets, it is common to observe a "cooperative paramagnetic" regime, in which the dominant exchange interactions impose strong constraints on the spin configurations, but the spins still manage to remain strongly fluctuating. The "spin ice" materials, in which rare-earth Ising moments locally satisfy Pauling's ice rules, provide a prominent and beautiful set of examples, which have stimulated a rich interplay between theory and experiment. Constraints on the spin phase space have been implicated in the physics of diverse other magnetic materials, such as the spinel chromites[1] and the A-site diamond antiferromagnetic spinels.[2]

Generally, residual interactions, subdominant to those responsible for the constraints, lead to a quenching of the remaining fluctuations. To quantify this, we may associate the dominant interactions with a temperature, T_0, below which the constraints are well satisfied and the system is highly correlated. We will assume that fluctuations among the constrained states are removed at another temperature $T_c \ll T_0$, which is determined by subdominant effects. Often, this quenching of the constrained fluctuations is associated with a symmetry breaking, such as magnetic ordering or lattice deformation. This phase transition occurs in a very different environment from conventional order-disorder transitions, in which the high-temperature phase is a weakly correlated paramagnet. Here, the strong constraints imply strong correlations in the cooperative paramagnet. It has recently been appreciated that such correlations can drastically affect phase transition(s).[3–6] Transitions can be induced where none would otherwise be present, and furthermore, symmetry-mandated transitions may be modified from their usual Landau-Ginzburg-Wilson (LGW) universality classes.

In this paper, we explore these phenomena in a large set of classical dimer models on the cubic lattice. Such dimer models are defined by a constrained phase space consisting of close-packed dimer coverings, in which dimers occupy (some) links of the lattice and the constraint is that each site is overlapped by one and only one dimer. In these models, the constraint is exactly satisfied, corresponding to the limit $T_0 \rightarrow \infty$. We expect that more realistic models are well approximated by this situation provided $T_c \ll T_0$. For models with a gap [of order of $O(k_B T_0)$] to states violating the constraint (as in spin ice), the approximation is in fact exponen-

tially good, since violations of the constraint occur with an Arrhenius probability $\propto \exp(-T_0/T_c)$.

In the cubic dimer models we study, a great deal is understood about the nature of the constraint induced correlations,[7] which have a power-law form. This can be cast (see Sec. IV) into a sort of pseudodipolar form, leading to the name "Coulomb phase" for the high-temperature $T > T_c$ region. Moreover, the dipolar correlations can be identified with an emergent Coulomb gauge field, similar to that appearing in true electromagnetism. Coulomb phases arise in a variety of other contexts;[8,9] for instance, the ice rules constraint related to spin ice also leads to a Coulomb phase.[9–12] For these types of systems, the gauge description has lead to some theoretical progress in understanding the consequent unconventional criticality. In such cases, the transitions are expected to involve dual "monopole" fields, which couple to the emergent gauge field and carry the associated gauge charge.[3,5] The full field theory therefore has a multicomponent Ginzburg-Landau form. The monopoles are "fractional" degrees of freedom in the sense that the symmetry-breaking order parameters (if any) are composites of these fields. We outline the derivation of this result in Sec. IV.

Though this construction of non-LGW critical theories has been discussed in some isolated instances previously, an unequivocal verification of the theory has proved difficult. In particular, the numerical experiments in Refs. 4 and 13, while providing evidence for unconventional criticality, are not in good quantitative agreement with the theoretical expectations. In particular, the numerical estimates[4] of various critical exponents, e.g., $\nu = 0.50(4)$, $\alpha = 0.56(7)$, and $\eta = -0.02(5)$, are indicative of an unexplained tricritical behavior.

In this paper, we perform a much more systematic investigation of a range of dimer models, in order to test the theoretical picture on a grander scale, in which many *qualitative* comparisons are possible. We find that the gauge theory does an excellent job on these qualitative tests, providing understanding of the numerical results for nearly all cases.

A. Outline of models and results

Before going into a detailed discussion, we first provide a brief overview of the models we will study and our main results. We start by introducing a family of close-packed, classical dimer models on the cubic lattice. The elementary degrees of freedom in these models are hard-core dimers occupying the bonds of the cubic lattice with the constraint that every site in the lattice is part of exactly one such dimer. We further introduce a (potential) energy scale favoring dimer coverings with parallel dimers on neighboring bonds. At low temperature, these models exhibit long-range columnar order of the dimers. In general, there are six distinct columnar ordering patterns that can maximize the number of parallel dimers on neighboring bonds as illustrated in Fig. 1.

The main distinction between the various models we will consider then comes from a selection of a subset of these energetically favored ordering patterns. The Hamiltonian of a parent model that favors all six possible ordering patterns
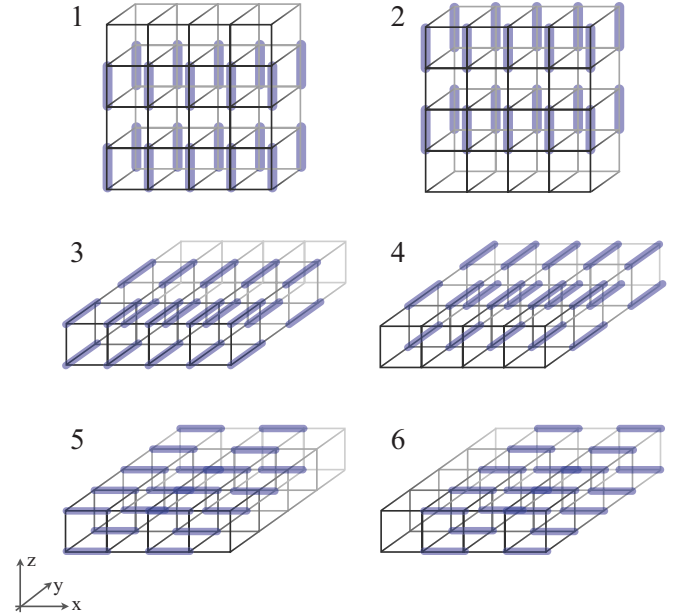
FIG. 1. (Color online) The six dimer coverings with columnar dimer ordering that maximize the number of parallel dimers on neighboring bonds of the cubic lattice. Our family of classical dimer models energetically favors these ordering patterns with the 6-GS model favoring all six states, the 4-GS model favoring states 3–6, the 2-GS model favoring states 1–2, and the 1-GS model favoring a single state only. Further variations are discussed in the text.

and which we therefore call the "6-GS" model is given by

$$\mathcal{H}_{6\text{-GS}} = -\sum_{\square} (n_= + n_{/\!/} + n_{\parallel}). \qquad (1)$$

Here $n_=$, $n_{/\!/}$, and $n_{\parallel}$ count the number of parallel dimers on neighboring bonds along the x, y, z lattice directions and the sum runs over all square plaquettes of the cubic lattice.

Our first family of dimer models selects particular subsets of four, two, and one columnar dimer coverings as ground states. The "4-GS" model favors the four columnar states in x and y directions, e.g., states 3–6 in Fig. 1, and is described by the Hamiltonian

$$\mathcal{H}_{4\text{-GS}} = -\sum_{\square} (n_= + n_{/\!/}). \qquad (2)$$

The "2-GS" model favors columnar orderings only along one lattice direction, say the z direction, e.g., states 1–2 in Fig. 1, with Hamiltonian

$$\mathcal{H}_{2\text{-GS}} = -\sum_{\square} n_{\parallel}. \qquad (3)$$

While these two models have somewhat different ground-state properties, they will turn out to exhibit rather similar physics. More specifically, they share the same set of symmetries, which we will discuss in detail in Sec. IV A 2. The last member of this first family of models is the "1-GS" model which singles out one of the six columnar orderings as sole ground state. We choose one of the columnar orderings in the z direction and define $n_{\parallel}^{e/o}$ to be the number of

plaquettes with parallel dimers on neighboring even or odd bonds, respectively. Then the Hamiltonian of the 1-GS model can be written as

$$\mathcal{H}_{1\text{-GS}} = -\sum_{\square} n_{\parallel}^{e}. \tag{4}$$

A common feature of all four models introduced above is that they all undergo a *direct* thermal transition between the Coulomb gas phase at high temperature and a conventional long-range ordered state at low temperature as we will discuss in Sec. II. Our parent Hamiltonian, the 6-GS model, has first been studied in Ref. 4, where based on an extensive numerical analysis, the authors argue that this model undergoes a *continuous* thermal transition with the system spontaneously selecting one of the six columnar ordering patterns at the transition out of the Coulomb phase. Our present numerical analysis for the other three models indicates that the 2-GS and 4-GS models exhibit (strongly) first-order transitions, while we find strong evidence that the transition of the 1-GS model is again continuous.

In Sec. III, we provide further numerical evidence for the continuous nature of the 1-GS model by embedding this transition into a line of continuous transitions for systems of identical symmetry. The latter is achieved by studying a continuous interpolation of the 1-GS and 2-GS models in Sec. III A. A similar approach interpolating the 4-GS to 6-GS models is given in Sec. III B.

To understand the different phase transitions found numerically, we develop candidate field theories in Sec. IV. To this end, we first rewrite the dimer models in terms of a compact $U(1)$ gauge theory. A subsequent duality transformation then allows to make the monopole excitations in this gauge theory explicit and describe the phase transitions as Higgs confinement transitions driven by the condensation of monopoles. Finally, the candidate field theories are derived in terms of two complex fields (a CP^1 field) coupled to a $U(1)$ gauge field. The symmetry-mandated Landau-Ginzburg actions for the various dimer models are given in Sec. IV B and implications for the phase transitions are discussed. In particular, this analysis suggests that the 1-GS model undergoes a continuous transition in the three-dimensional (3D) inverted *XY* universality class, while the 2-GS model should undergo a first-order transition. While analytically inferring the nature of the transition for the 4-GS and 6-GS models is somewhat more delicate as discussed in Sec. IV B, we find an overall good agreement with the numerical results.

In Sec. V, we discuss a second family of dimer models with the common characteristic that there are two subsequent thermal transitions between the Coulomb phase and the dimer crystal. As a representative model, we discuss the so-called "*xy*" model in some detail, which favors one columnar ordering pattern along the x and y lattice directions, respectively. We find that the system first undergoes a continuous Higgs transition out of the Coulomb phase, which again is in the 3D inverted *XY* universality class and subsequently a first-order "spin-flop" transition to the dimer crystal. We give some concluding remarks in Sec. VI on the general interest of these classical dimer models in the search of non-LGW phase transitions.

II. MONTE CARLO SIMULATIONS

A. Overview

We first summarize some characteristic numerical results for the thermal transitions obtained from extensive Monte Carlo simulations. The classical nature of our models not only commands to use an efficient stochastic algorithm to traverse the space of dimer coverings, but also allows for nonlocal update schemes such as the worm algorithm.[14,15] The latter performs an update by flipping a whole sequence of dimers when moving from one dimer covering to another one, which drastically reduces the problem of critical slowing down close to phase transitions. In more technical terms, we used so-called heat-bath transition rates to perform the local worm updates (at all temperatures), which are described in detail in Refs. 14 and 15.[34] For all parameter choices, we typically ran 10^5 thermalization sweeps and then collected Monte Carlo estimates from multiple parallel runs typically recording some 10^6 measurements. We used this algorithm on samples with $N = L^3$ sites up to 256^3—sizes which sometimes turn out to be necessary to ascertain the nature of a phase transition.

The update scheme of the worm algorithm further allows sampling the behavior of two test monomers embedded in the dimer coverings. In particular, the update is performed by initially breaking up an arbitrary dimer into a pair of monomers and then moving one monomer across the lattice by flipping dimers along a string or "worm" until it can be recombined with the other monomer into a newly formed dimer. This construction can be used to reveal the confining properties of the low-temperature phases in our dimer models. To this end, we define the monomer "confinement length" $\xi^2(T)$ as the (squared) average distance between the two test monomers, which we rescale by the expectation value $(L^2+2)/4$ for deconfined monomers moving freely on the lattice for a finite cube of even linear extent L (and periodic boundary conditions).

We also measure thermodynamical quantities such as the internal energy $E(T)$, the specific heat $C_v(T) = (\langle E^2 \rangle - \langle E \rangle^2)/T^2$, as well as the stiffness ρ. The stiffness encodes fluctuations of dimer fluxes: $\rho = \sum_{\alpha = x,y,z} \langle \phi_\alpha^2 \rangle / 3L$, where the flux ϕ_α is the algebraic number of dimers crossing a plane perpendicular to the unit vector $\vec{e}_\alpha$. Algebraic here means that, given a lattice direction, we count +1 for a dimer going from one sublattice to the other and −1 for the reverse situation. Fluxes ϕ_α are conserved quantities (plane by plane) which vanish on average for symmetry reasons.

In Fig. 2 we plot the specific heat per site $C_v(T)/N$, the energy per site $E(T)/N$, and the monomer confinement length $\xi^2(T)$ for the four models introduced in the previous section.

For all four models, we find clear thermodynamic signatures for a direct transition between the high-temperature Coulomb phase (with deconfined monomers) to the dimer crystal at low temperatures (with confined monomers). The sharp, kinklike features in the energy $E(T)$ and monomer confinement length $\xi^2(T)$ are indicative of a first-order transition for the 2-GS and 4-GS models. The first-order nature

specific heat

energy

confinement length
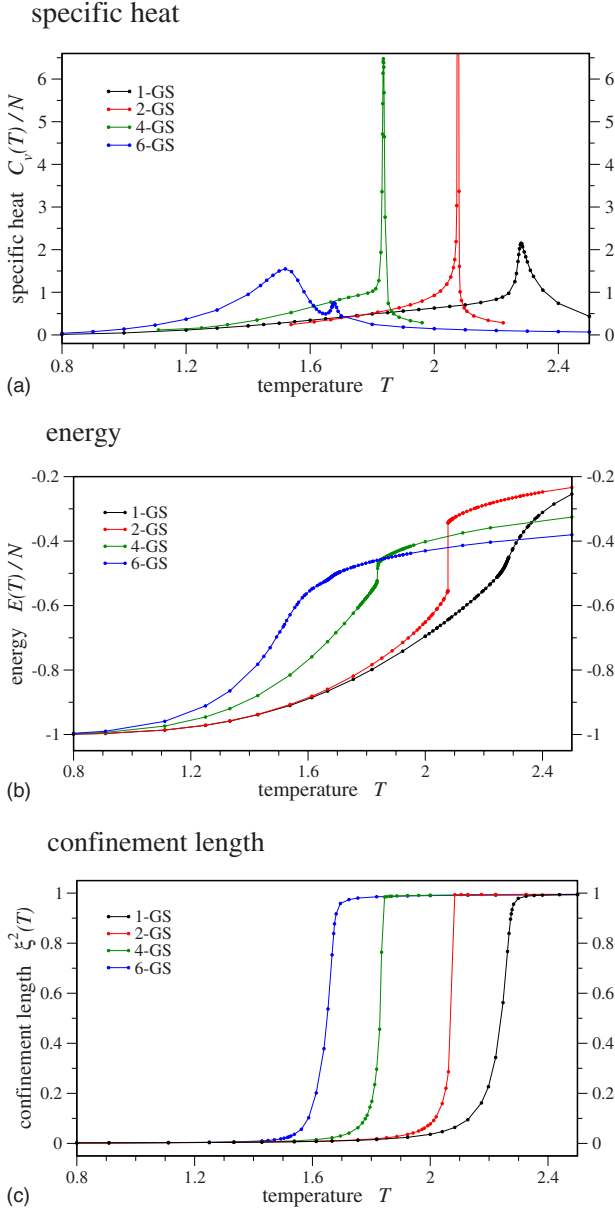
FIG. 2. (Color online) Overview of numerical results for the dimer models with one (1-GS), two (2-GS), four (4-GS), and six (6-GS) columnar ground states: (a) the specific heat per site $C_v(T)/N$, (b) the energy per site $E(T)/N$, and (c) the monomer confinement length $\xi^2(T)$ defined in the text. All four models undergo a direct transition with clear thermodynamic signatures between the high-temperature Coulomb phase (with deconfined monomers) to the dimer crystal at low temperature (with confined monomers). The sharp, kinklike features in the energy $E(T)$ and monomer confinement length $\xi^2(T)$ are indicative of a first-order transition for the 2-GS and 4-GS models. The 1-GS and 6-GS models undergo continuous transitions with smooth features. Data are shown for system size $L=48$ for the 1-GS and 6-GS models and $L=32$ for the 2-GS and 4-GS models.

of these transitions is fully revealed in bimodal energy histograms in the vicinity of the transition temperature, which we will discuss in detail in Sec. III. The 1-GS and 6-GS models exhibit smooth features in the energy $E(T)$ and monomer confinement length $\xi^2(T)$ and a (divergent) peak in
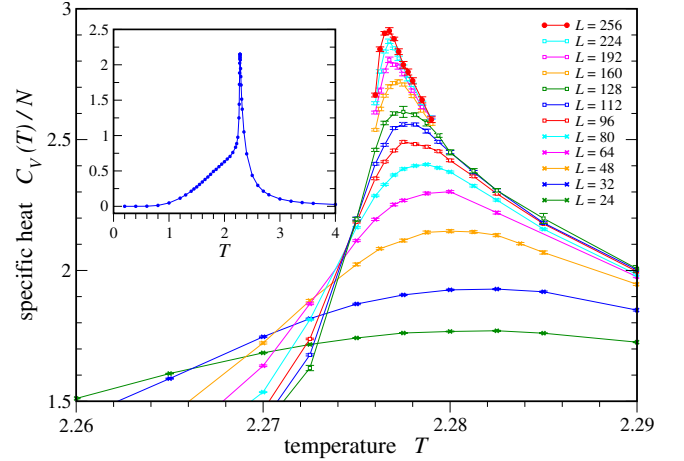
FIG. 3. (Color online) Specific heat per site $C_v(T)/N$ for the 1-GS model as function of temperature T and different system sizes L. Inset shows a specific-heat scan over a wide temperature range for a sample $L=48$ system size. Below the peak around $T_c \approx 2.276 \pm 0.001$, there is a shoulder which shows no variation with system size.

the specific heat $C_v(T)$ which are indicative of a continuous phase transition. While we will not discuss the 6-GS model in detail here and refer to previous work in Ref. 4, we unambiguously demonstrate in the following that the 1-GS model undergoes a continuous transition in the 3D *XY* universality class. We will now turn to the individual dimer models and discuss our numerical results in more detail in the following.

B. 1-GS model

We will first concentrate on the 1-GS model which energetically favors a single columnar dimer ordering pattern shown in Fig. 1. Our numerical simulations for systems with up to 256^3 lattice sites clearly suggest that this model undergoes a *continuous* thermal transition between the Coulomb phase and the dimer crystal.

The specific heat plotted in Fig. 3 exhibits a peak around the transition temperature of $T_c \approx 2.276 \pm 0.001$ that diverges very slowly with L. Below this peak, there is a shoulder that does not show any variation with system size (see inset of Fig. 3) and thus cannot be associated with any long distance or critical behavior. The latter is reminiscent of the 6-GS model[4] which below the transition temperature exhibits an even more pronounced shoulder (for a comparison, see also Fig. 2).

A distinct feature of the Coulomb phase is that (test) monomers are deconfined. As a consequence, we expect the monomers to confine at the phase transition out of the Coulomb phase. This confinement transition can be tracked using the monomer confinement length $\xi^2(T)$ introduced above. Plotting data for various systems sizes, as shown in Fig. 4, reveals a distinct crossing point at the transition temperature. This absence of finite-size effects at the transition temperature indicates a universal value of the confinement length $\tilde{\xi}(T_c)$ at this transition, which we estimate to be
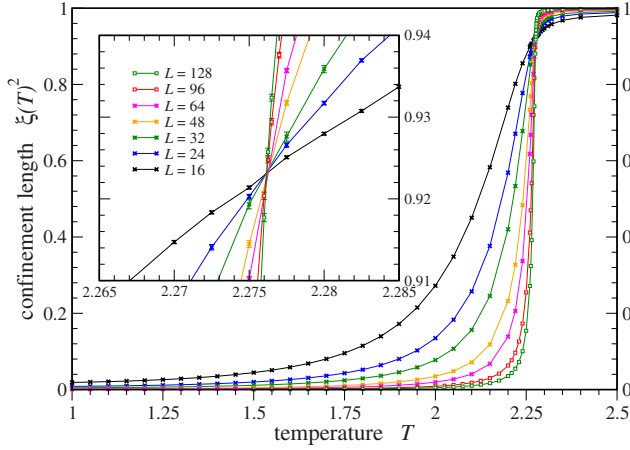
FIG. 4. (Color online) Confinement length $\xi^2(T)$ for the 1-GS model measuring the (squared) average distance between two monomers. Data for different system sizes L are renormalized by the expectation value $(L^2+2)/4$ for deconfined monomers. The distinct crossing point shown in the inset for temperatures in the vicinity of the transition temperature indicates a continuous transition.

$\widetilde{\xi}(T_c) \approx 0.923 \pm 0.001$. This crossing point strongly indicates a continuous transition.

Another indication of a continuous transition is that the distribution of dimer fluxes ϕ also becomes universal at the transition temperature. Indeed curves of the stiffness ρ (multiplied by system size L) cross for different L at the transition out of the Coulomb phase, as shown in Fig. 5. The position of this crossing point coincides exactly with the transition temperature $T_c=2.276 \pm 0.001$ estimated from the specific heat.

Having established the continuous nature of the transition, we now turn to its universality class. Since this phase transition occurs without any spontaneous symmetry breaking, we cannot rely on conventional techniques using an order parameter to measure critical exponents. However, we can still consider thermodynamics, such as the behavior of the specific heat in the vicinity of the transition. As shown in
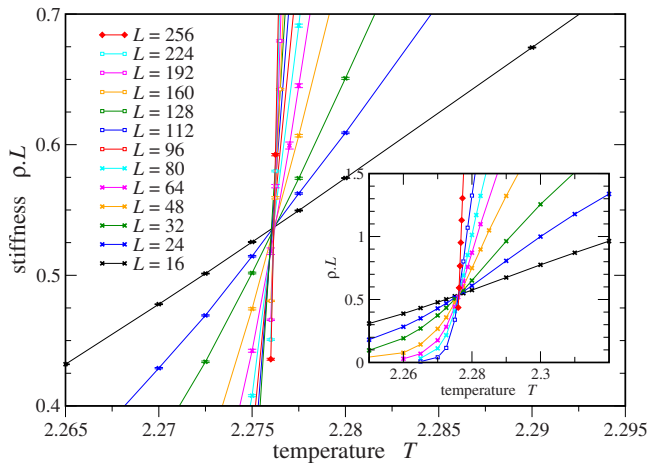
FIG. 5. (Color online) Stiffness ρ of the 1-GS model multiplied by L vs temperature T near the transition for different system sizes L. The crossing point indicates a continuous transition.
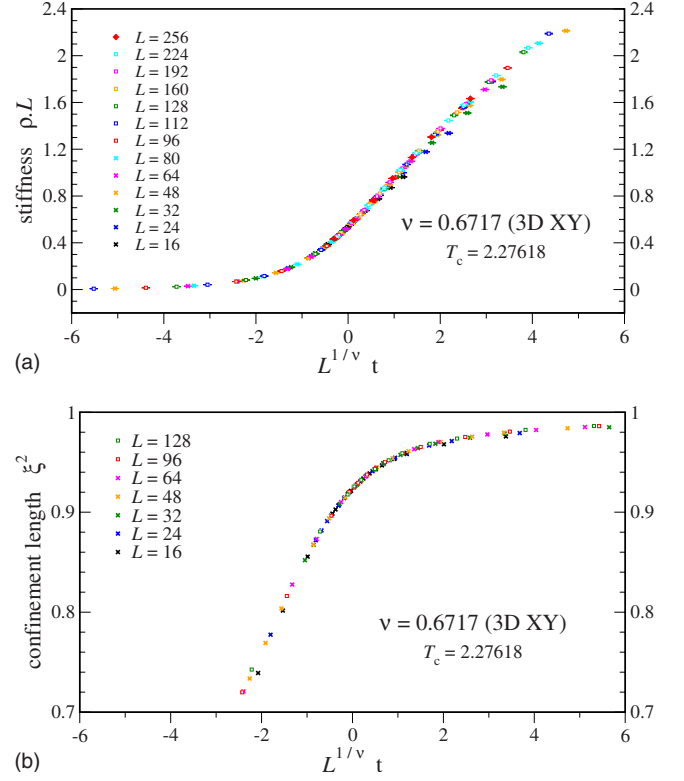
FIG. 6. (Color online) Data collapse for the stiffness ρ multiplied by L (top panel) and confinement length ξ^2 (lower panel) of the 1-GS model as a function of $L^{1/\nu}t$, where $t=(T-T_c)/T_c$, with $T_c=2.276\,18$. The critical exponent $\nu=0.6717$ corresponds to the 3D XY universality class.

Fig. 3, $C_v(T_c)/N$ grows very slowly with system size at criticality, which would suggest a critical exponent $\alpha > 0$, but very small. It is also quite possible that $C_v(T_c)/N$ actually converges to a finite value, but for system sizes that are currently out of reach of our numerical simulations. This would indicate a negative value for $\alpha < 0$, also likely very small. This latter scenario is not unlikely considering the 3D XY model, which is known to have a small negative critical exponent $\alpha=-0.0151$,[16] but for which numerical simulations[17] do not see a convergence of the specific heat.

Thermodynamics being of little help to determine the universality class, another possibility is to consider crossings and data collapse of adequate quantities, including the stiffness and the confinement length. Standard finite-size scaling arguments indicate that close to the transition point, the stiffness should scale as $\rho=\frac{1}{L}\widetilde{\rho}(L^{1/\nu}t)$, where $\widetilde{\rho}$ is a universal function, $t=(T-T_c)/T_c$ the deviation from the critical temperature, and ν the correlation length exponent. Performing this analysis, we find a nice data collapse for the correlation length exponent $\nu=0.6717$ of the 3D XY universality class[16] as shown in the top panel of Fig. 6. The same scaling form $\xi=\widetilde{\xi}(L^{1/\nu}t)$ is also expected for the confinement length ξ^2. As shown in the lower panel of Fig. 6, we again find a data collapse for the same exponent $\nu=0.6717$. Finally, we note that the system-size independent value $\widetilde{\xi}(T_c) \approx 0.923 \pm 0.001$ is another characteristic of the universality class of the transition and in this case also points to the 3D XY universality class.[18]
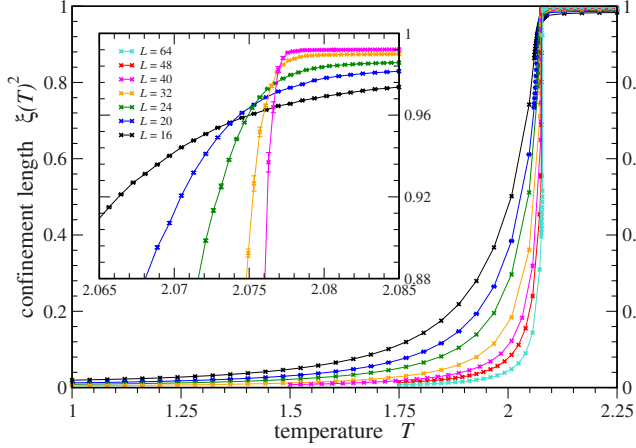
FIG. 7. (Color online) Confinement length $\xi^2(T)$ for the 2-GS model. Data for different system sizes L are renormalized by the expectation value $(L^2+2)/4$ for deconfined monomers. The absence of a distinct crossing point in the vicinity of the transition temperature indicates a first-order transition.

C. 2-GS and 4-GS models

We contrast our finding of a continuous transition in the 1-GS model to numerical results for the 2-GS and 4-GS models which both undergo first-order transitions between the Coulomb phase and the dimer crystal phase. In Figs. 7 and 8, the confinement length of monomers is plotted. Similar to the 1-GS model, the transition out of the Coulomb phase is accompanied with a confinement of the monomers. At these first-order transitions, however, there is no distinct crossing point (see insets of Figs. 7 and 8).

III. CONTINUOUS INTERPOLATION BETWEEN DIMER MODELS

One way to firmly establish the continuous nature of the phase transition in the 1-GS and 6-GS dimer models is to
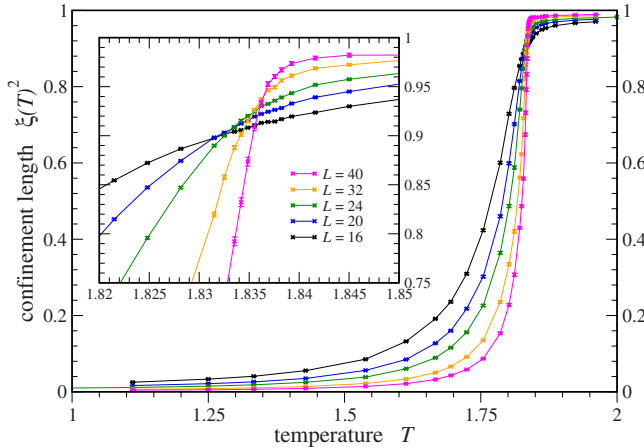
FIG. 8. (Color online) Confinement length $\xi^2(T)$ for the 4-GS model. Data for different system sizes L are renormalized by the expectation value $(L^2+2)/4$ for deconfined monomers. The absence of a distinct crossing point in the vicinity of the transition temperature indicates a first-order transition.
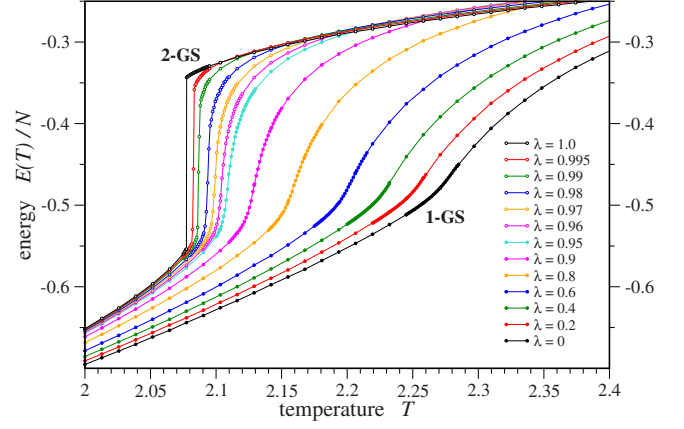
FIG. 9. (Color online) Energies per site for a dimer model which continuously interpolates between the 1-GS ($\lambda=0$) and 2-GS ($\lambda=1$) models. Data shown are for system size $L=48$.

demonstrate that these transitions can be embedded into *lines* of continuous transitions. We will first concentrate on the 1-GS model and show that such a line of continuous transitions ending in a proposed, multicritical point can indeed be found. We will then discuss a similar idea for the 6-GS model, which however does not reveal such a line of continuous transitions.

A. Interpolating the 1-GS and 2-GS models

We have already observed that the 1-GS model which favors a single columnar ordering pattern in one lattice direction undergoes a continuous transition, while the 2-GS model which favors the two possible columnar ordering patterns in a given lattice direction undergoes a strong first-order transition. We can now ask how the nature of the phase transition changes as we continuously interpolate between these two models. To this end, we continuously vary the weights for the columnar ordering patterns on the odd/even bonds in a given lattice direction. Formally, we introduce a coupling parameter λ with $0\leq\lambda\leq1$ on every other bond

$$\mathcal{H}_{1\text{-}2\text{-GS}} = -\sum_{\square}(\lambda n_\parallel^o + n_\parallel^e). \tag{5}$$

For $\lambda=0$, we recover the 1-GS model, while $\lambda=1$ corresponds to the 2-GS model.

Our numerical simulations for various interpolation parameters λ are summarized in Figs. 9 and 10, which show the energy per site $E(T)/N$ and histograms of the energy per site in the vicinity of the transition temperature, respectively. Starting from the 2-GS model ($\lambda=1$) the sharp, kink-like feature in the energy accompanying the first-order transition quickly vanishes for interpolation parameters $\lambda<1$ as the two possible columnar dimer orderings acquire different weights. The energy histograms in the vicinity of the transition temperatures turn from a bimodal distribution in the parameter regime $1\geq\lambda\gtrsim0.97$ into a single peak distribution for $\lambda<0.97$ and system size $L=48$ (see Fig. 10). The first-order transition of the 2-GS model turns continuous for some intermediate λ, which for larger system sizes might be closer
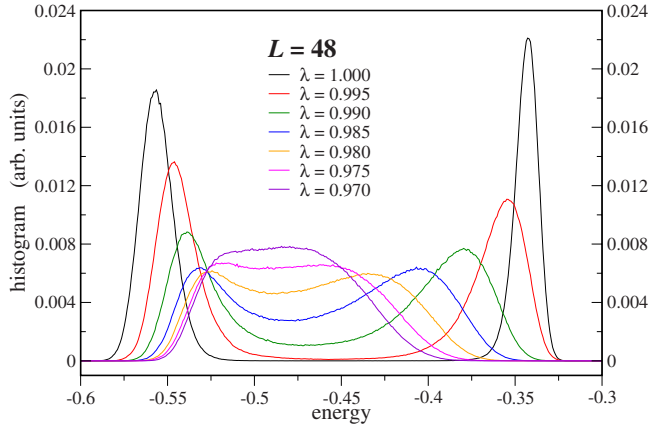
FIG. 10. (Color online) Energy (per site) histograms for the dimer model interpolating between the 1-GS and 2-GS models in the vicinity of the transition temperature of the respective models. Data shown are for system size $L=48$.

FIG. 11. (Color online) Energies per site for a dimer model which continuously interpolates between the 4-GS ($\lambda=0$) and 6-GS ($\lambda=1$) models. Data shown are for system size $L=48$.

to $\lambda_c \approx 0.95$. On the other hand, this demonstrates that the continuous transition of the 1-GS model is indeed part of a line of continuous transitions which extends over the range $0 \leq \lambda \leq \lambda_c$ and likely ends in a *multicritical* point at λ_c. Note that while $\lambda \neq 1$ introduces a staggering with respect to the two columnar ordering patterns, the system exhibits identical symmetries for all $0 \leq \lambda < 1$, which will lead to a uniform theoretical description of the interpolated models for all $0 \leq \lambda < 1$. However, since the strong first-order transition of the 2-GS is expected to be stable toward a small perturbation $\delta \lambda = 1 - \lambda$, it is not surprising to see that the interpolated models exhibit (weak) first-order transitions in the regime $0.97 \lesssim \lambda \leq 1$, but quickly turn to uniform behavior for smaller λ.

B. Interpolating the 4-GS and 6-GS models

We now turn to the 6-GS model, for which we can study a similar interpolation to the 4-GS model, which in contrast to the 6-GS model undergoes a first-order transition. Again, we introduce an interpolation parameter λ which now assigns different weights to the two columnar ordering patterns that establish the difference between the 4-GS and 6-GS models. Formally, we investigate the Hamiltonian

$$\mathcal{H}_{4-6\text{-GS}} = -\sum_{\square} (n_= + n_{/\!/} + \lambda n_{\|}), \qquad (6)$$

with $0 \leq \lambda \leq 1$. For $\lambda=0$, this is the 4-GS model, while $\lambda=1$ now corresponds to the 6-GS model.

Our numerical results for various interpolation parameters λ are summarized in Figs. 11–13, respectively. A sharp, kink-like feature around the transition temperature in the energy $E(T)$ persists for almost all interpolation parameters $0 \leq \lambda < 1$ (see Fig. 11). Energy histograms in Fig. 12 for the respective transition temperatures show bimodal distributions for the same parameter range. Pushing the limit of our calculations, we can establish a two-peak structure up to $\lambda=0.98$ for system size $L=96$ (see the lower panel in Fig. 12). Systematically tracing the distance between the two
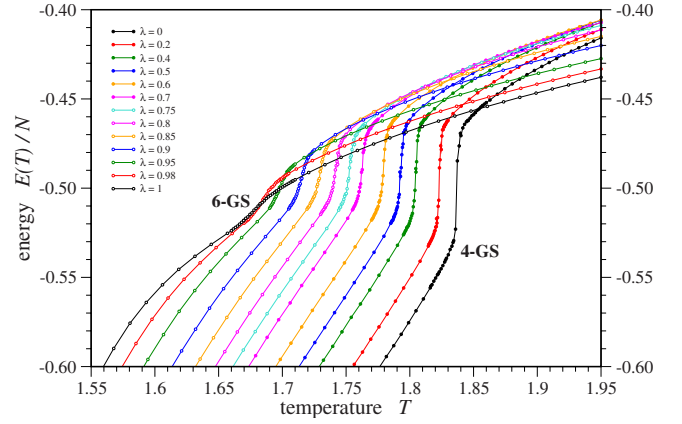
peaks in these bimodal energy distributions as shown in Fig. 13, the emerging trend clearly suggests that the line of first-order transitions persists all the way up to $\lambda < 1$. The transition weakens along this line to finally turn continuous for the 6-GS model, where we found no sign of a bimodal distribution for $\lambda=1$, in agreement with the conclusions of Ref. 4.

(a)

(b)
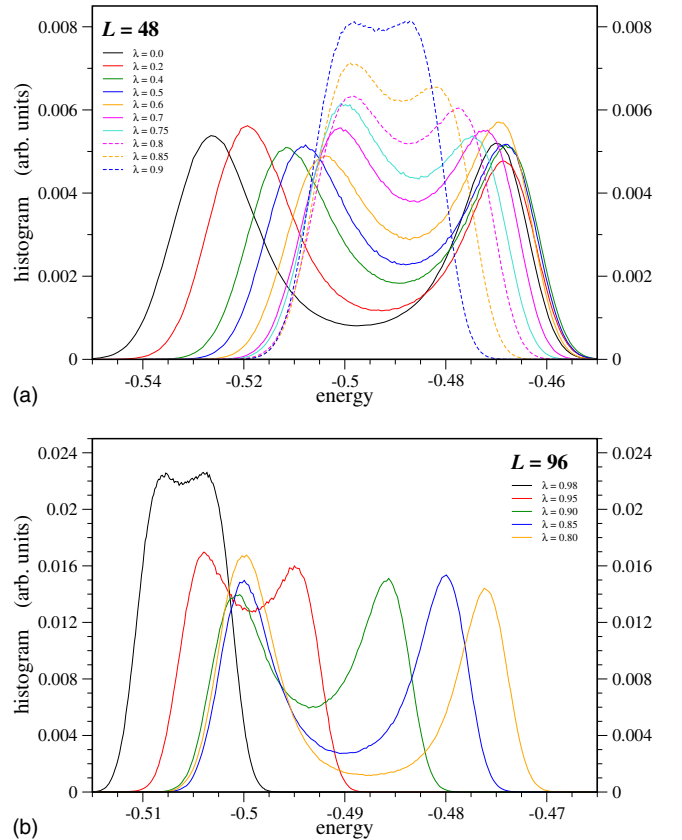
FIG. 12. (Color online) Energy (per site) histograms for the dimer model interpolating between the 4-GS and 6-GS models in the vicinity of the transition temperature of the respective models. Data shown are for system sizes $L=48$ in the upper panel and $L=96$ in the lower panel.
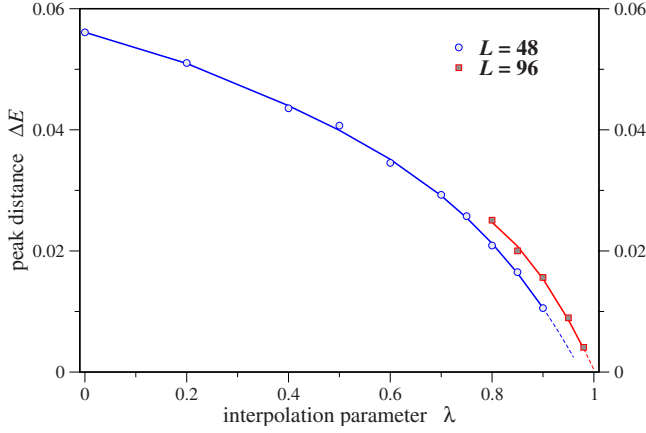
FIG. 13. (Color online) Distance between the two peaks in the bimodal energy histograms shown in Fig. 12. Lines are guides to the eyes. Data for system sizes $L=48$ and $L=96$ are shown.

IV. CANDIDATE FIELD THEORIES

To understand the different nature of the phase transitions discussed in Sec. II, we will now develop a family of candidate field theories describing these transitions. To do this, we take advantage of a pair of mappings: from the dimer model to compact lattice quantum electrodynamics (QED), and thence to a dual monopole formulation. The continuum limit of the latter leads directly to the desired field theories.

The desired mappings have been discussed in some detail in Refs. 3 and 19 and in fact can be performed not only for the classical dimer model discussed here but also its quantum generalization. For clarity, we will present in this section a brief, self-contained summary of the mapping in the classical case for the cubic lattice, applicable to the models of the present paper. Performing a detailed symmetry analysis, we then derive the symmetry allowed Ginzburg-Landau actions for the various models and discuss implications for their respective phase transitions.

A. Mappings

To proceed, we define a bond variable which counts the number of dimers on a given bond

$$
\hat{n}_{ab} = \begin{cases} 1, & \text{if the bond } \langle a,b \rangle \text{ is occupied by a dimer} \\ 0 & \text{otherwise.} \end{cases}
$$

$$(7)$$

The close-packed dimer constraint which requires that every site in the cubic lattice be part of exactly one dimer can then be expressed as

$$
\hat{N}_a \equiv \sum_b \hat{n}_{ab} = 1, \tag{8}
$$

where the sum is over sites b which are nearest neighbors of a. A monomer excitation in the dimer model which breaks the close-packing constraint, e.g., an unpaired site a on the cubic lattice, is then indicated by $\hat{N}_a=0$.

1. Compact QED

We may directly pass to QED variables as follows. We introduce an electric field variable E_{ab}, which is a directed variable, according to

$$
E_{ab} = \epsilon_a \hat{n}_{ab}, \tag{9}
$$

where E_{ab} is integer valued (in particular $E_{ab}=0, \pm 1$) and we have introduced a "background charge" ϵ_a with a fixed distribution of alternating charges on the two sublattices

$$
\epsilon_a = \begin{cases} +1, & a \in \text{A sublattice} \\ -1, & a \in \text{B sublattice.} \end{cases} \tag{10}
$$

In the QED formulation, the local constraint (8) maps directly to a lattice version of the Gauss law,

$$
\text{div } \vec{E} = \epsilon_a, \tag{11}
$$

which also explains the notion of the background charge and where we have used the lattice divergence div $\vec{E} = \Sigma_b E_{ab}$.

Expressed in the QED variables, the Hamiltonian becomes

$$
\mathcal{H}_{\text{QED}} = \frac{U}{2} \sum_{\langle a,b \rangle} \left(E_{ab} - \frac{\epsilon_a}{2} \right)^2 - \sum_{\square} \left(\delta_{\text{curl } \vec{E},2} + \delta_{\text{curl } \vec{E},-2} \right) + \text{const,}
$$

$$(12)$$

where the first term is a constant in the physical space in which $\hat{n}_{ab}=0,1$. We include it, however, in order that we may allow the electric variable E_{ab} to fluctuate over *all* integers; by taking the large U limit, the physical dimer states, which minimize this term, are selected. It is expected that the universal properties of $\mathcal{H}_{\text{QED}}$ are identical for infinite and finite U.

Note that the Hamiltonian (12) is rather similar to the standard formulation of compact QED. The main difference is the absence of any magnetic field terms B^2, which reflects the classical nature of the dimer model under consideration, a shifting of the E^2 term by an alternating "background field" $\epsilon_a/2$, and the energetic preference for curl $\vec{E} = \pm 2$. Despite these differences, Hamiltonian (12) does share all the same internal symmetries as the more conventional QED form. It is therefore expected to share the same properties in regimes where universality is mandated.

2. Duality, monopole formulation, and symmetry transformation

In contrast to a conventional, noncompact QED formulation, a *compact* QED such as the one introduced in Sec. IV A 1 does *not* prohibit magnetic monopoles. These monopoles are "conjugate" to the gauge charges in the QED description, which in terms of the original dimer models correspond to monomer excitations. The defining characteristic of the Coulomb phase is that the gauge charges are *deconfined*, while the magnetic monopoles are well-defined, gapped quasiparticles. In the dimer crystal phase, on the other hand, the electric charges are confined and the electric field is static. This implies that the conjugate magnetic field is strongly fluctuating and the magnetic monopoles are no longer good excitations. We can thus describe the phase transition out of
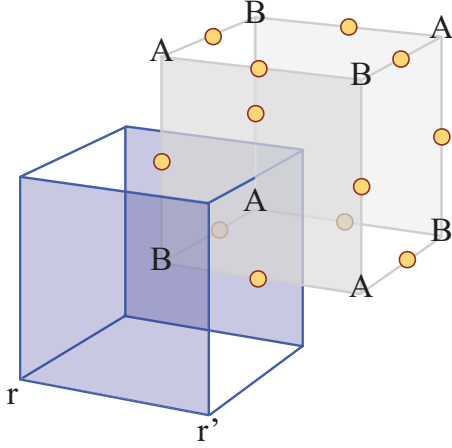
FIG. 14. (Color online) Cubic lattice and its dual. The dual cubic lattice sites sit at the centers of each cube of the cubic lattice.

the Coulomb phase as the (Bose) condensation of magnetic monopoles accompanied by a simultaneous confinement transition of the electric charges.

Our goal now is to establish an analytic description of this phase transition in terms of the magnetic monopoles. To this end, we will first introduce a duality transformation to make the monopole excitations explicit in the Coulomb phase. It is well known that the electric and magnetic fields in Maxwell's equations are dual in the *absence* of charges and currents. However, while there are no currents in our system, there is a nonvanishing charge distribution, as given by the nonvanishing electric field divergence in Eq. (11). We therefore introduce a "background electric field" $\vec{e}^{(0)}$, which compensates for these background charges by satisfying

$$\text{div } \vec{e} = \epsilon_a \qquad (13)$$

and making $\vec{E} - \vec{e}$ divergence free. Note that while $\vec{E}$ is a fluctuating variable, the background field $\vec{e}$ is static. It is convenient to choose $\vec{e}$ to be integer valued for what follows. Then a simple choice to satisfy Eq. (13) is to place $e_{a,a+\hat{x}} = (1 + \epsilon_a)/2$ on the link emanating in the x direction from site a.

This allows us to write down a duality transformation of the form

$$\vec{E}_{ab} = -\text{curl } \vec{\alpha} + \vec{e}_{ab}, \qquad (14)$$

where we have introduced a dual electric vector potential $\vec{\alpha}$. In a quantum theory, $\vec{\alpha}$ would generate the conjugate magnetic field. Due to the integer constraint on $\vec{E}_{ab}$, we must also take $\vec{\alpha}$ to be integer valued (this reflects our integer choice of $\vec{e}_{ab}$).

In terms of these dual variables, the QED Hamiltonian (12) becomes

$$\mathcal{H}_{\text{dual-QED}} = \frac{U}{2} \sum_{\square} \left(\text{curl } \vec{\alpha} - \vec{e} + \frac{\epsilon_a}{2} \right)^2 - \sum_{\langle ab \rangle} F[\nabla^2 \alpha],$$
$$(15)$$

where the squares "$\square$" now denote the plaquettes of the dual cubic lattice (see Fig. 14) and the last term $F[\nabla^2 \alpha]$ represents

the transcription of the last term in Eq. (12) in terms of $\vec{\alpha}$. We will not need its explicit form here. It is only important to note that it contains *second-order* (lattice) derivatives of the vector potential $\vec{\alpha}$. Upon coarse graining, such terms are irrelevant in the continuum limit. What is important is that, in the process of integrating out short scale fluctuations, they will generate relevant terms of all possible types dictated by symmetry. In this way, the physics of the dimer interactions, which is reflected in the F function, enters the low-energy continuum field theory description.

We now proceed to develop the continuum limit, following a sequence of standard manipulations.[20] In doing so, we will neglect the F term, on the grounds discussed above, keeping in mind that in the final continuum theory, we must restore all possible symmetry-allowed interactions that may be generated from it. We first soften the integer constraint on the vector potential $\vec{\alpha}$, replacing the constraint by a term which favors integer values. This approximation does not change the nature of the monopole-condensing phase transition. We rewrite the Hamiltonian (15) as

$$\mathcal{H} = \frac{U}{2} \sum_{\square} (\text{curl } \vec{\alpha} - \vec{e})^2 - w \sum_{r,r'} \cos[2\pi \alpha_{r,r'}], \qquad (16)$$

where large w recovers the integer α constraint. With this rewriting, we may regard α as a real-valued variable. In the first term, we have also *dropped* the $\epsilon_a/2$ term found inside the parenthesis of the first term in Eq. (15). This is possible because this term, regarded as a vector field, is purely longitudinal (i.e., curl free) and, hence, actually decoupled from the curl $\vec{\alpha}$ factor. We will soon extract a further longitudinal piece from e.

To proceed, we first introduce explicit monopole phase variables by making the gauge transformation $\alpha_{rr'} \to \alpha_{rr'} - (\theta_r - \theta_{r'})/2\pi$. One obtains

$$\mathcal{H} = \frac{U}{2} \sum_{\square} (\text{curl } \vec{\alpha} - \vec{e})^2 - w \sum_{r,r'} \cos[\theta_r - \theta_{r'} - 2\pi \alpha_{r,r'}].$$
$$(17)$$

Next, we break the background field e into transverse and longitudinal parts,

$$\vec{e} = \vec{e}_L + \vec{e}_T, \qquad (18)$$

such that div $\vec{e}_T = 0$ and curl $\vec{e}_L = 0$. Note that, because of the curl in Eq. (17), only $\vec{e}_T$ couples to $\vec{\alpha}$. Taking the divergence of Eq. (18), we see that div $\vec{e}_L = $ div $\vec{e} = \epsilon_a$. A choice for $\vec{e}_L$ satisfying this condition *and* which is curl free is simply

$$(e_L)_{a,a+\mu} = \epsilon_a/6. \qquad (19)$$

From this, we of course can find e_T by solving Eq. (18),

$$(e_T)_{a,a+\mu} = \frac{1}{2}(1 + \epsilon_a)\delta_{\mu,x} - \epsilon_a/6. \qquad (20)$$

Inserting Eq. (18) into Eq. (17) and dropping the decoupled and constant e_L part, we find

$$\mathcal{H} = \frac{U}{2}\sum_{\square}(\text{curl }\vec{\alpha} - \vec{e}_T)^2 - w\sum_{r,r'}\cos[\theta_r - \theta_{r'} - 2\pi\alpha_{r,r'}].$$

(21)

At this point, we have obtained a lattice Ginzburg-Landau theory, in which $\vec{e}_T$ appears as the (average) dual flux (experienced by the monopoles) through the dual plaquette pierced by this vector, expressed in units of the flux quantum. As usual, only the fractional part of the flux has physical significance. From Eq. (20), we readily see that this fractional part is uniformly 1/6 of a full flux quantum piercing the dual plaquettes emanating from one sublattice of the direct lattice and ending in the other. This can be seen as an array of alternating dual monopole fluxes, representing the original alternating ϵ_a background charges in the QED theory.

Precisely, this problem, of monopoles moving in this background flux pattern on the cubic lattice, was studied by Motrunich and Senthil in Ref. 19. We can adapt their results directly. We define a soft-spin monopole field $\psi_r \sim e^{i\theta_r}$ and neglect at first the fluctuations in the gauge field, replacing $\alpha_{rr'}$ by a static gauge configuration $\bar{\alpha}_{rr'}$ representing the background flux. The soft-spin Hamiltonian is

$$\mathcal{H}_{\text{monopoles}} = -w\sum_{\langle r,r'\rangle}[\psi_{r'}^{\dagger}\psi_r e^{-2\pi i\bar{\alpha}_{r,r'}} + \text{H.c.}].$$

(22)

Next we take the continuum limit, following Sec. VIB of Ref. 19. The hopping Hamiltonian in Eq. (22) has two minima, which we will call $\Psi_1(r)$ and $\Psi_2(r)$ here. A solution of the tight-binding Hamiltonian then becomes a linear combination

$$\psi(r) = \phi_1\Psi_1(r) + \phi_2\Psi_2(r),$$

(23)

where we treat ϕ_1 and ϕ_2 as slowly varying fields.

We can now ask how these solutions transform under the symmetry operations of the original cubic lattice. For the specific gauge choice of Ref. 19, these were reported to be

$$\begin{cases} T_x: & \phi_1 \to \phi_1^*, & \phi_2 \to -\phi_2^* \\ T_y: & \phi_1 \to \phi_1^*, & \phi_2 \to \phi_2^* \\ T_z: & \phi_1 \to \phi_2^*, & \phi_2 \to \phi_1^* \\ R_{\pi/2,Rxy}: & \phi_1 \to e^{-i\pi/4}\phi_1^*, & \phi_2 \to e^{i\pi/4}\phi_2^* \\ R_{\pi/2,Rxz}: & \phi_1 \to \frac{1}{\sqrt{2}}(\phi_1^* + \phi_2^*), & \phi_2 \to \frac{1}{\sqrt{2}}(\phi_1^* - \phi_2^*), \end{cases}$$

(24)

where the two 90° rotations $R_{\pi/2,Rxy}$ and $R_{\pi/2,Rxz}$ along the z and y lattice directions are around the sites on which the monopoles reside, e.g., the center of the cubes of the original cubic lattice or the sites of the dual lattice (see Fig. 14).

We have now established the symmetry transformation properties for the slowly varying fields in the solution of the gauge mean-field Hamiltonian (22). As we will describe in the next section, this allows us to make an explicit connection of these solutions to the individual members in our family of dimer models. In particular, we directly show how the

TABLE I. Symmetries of the various dimer models.

Dimer model	Symmetries
6-GS	T_x, T_y, T_z, $R_{\pi/2,Rxy}$, $R_{\pi/2,Rxz}$
4-GS	T_x, T_y, T_z, $R_{\pi/2,Rxy}$
2-GS	T_x, T_y, T_z, $R_{\pi/2,Rxy}$
1-GS	T_x, T_y, $R_{\pi/2,Rxy}$
xy	T_z, $R_{\pi/2,Rxy}$
xxy	T_x, T_y
xyz	$R_{\pi/2,Rxy}$, $R_{\pi/2,Rxz}$
$xyzz$	T_z, $R_{\pi/2,Rxy}$
$xxyyz$	T_x, T_y, $R_{\pi/2,Rxy}$

symmetries of the microscopic dimer interaction, implicitly contained in the appropriate F term in Eq. (15), re-enter the continuum field theory.

B. Effective Ginzburg-Landau actions and phase transitions

We will now turn to the individual members in our family of dimer models and derive an effective description in terms of a Ginzburg-Landau action that respects the symmetries of the various models. This action is typically given in terms of the two slowly varying complex fields ϕ_1 and ϕ_2 coupled to the dual $U(1)$ gauge field α_μ. We then analyze the derived actions and discuss the nature of the phase transitions in these field theories.

Let us first establish some notations and introduce a three-component vector $\vec{N}$, which will serve as an order parameter indicating which dimer ordering is chosen as the ground state

$$\vec{N}(\phi_1,\phi_2) \equiv \phi_\alpha^{\dagger}\vec{\sigma}_{\alpha\beta}\phi_\beta,$$

(25)

where $\vec{\sigma}$ are the three Pauli matrices. The six columnar ground states of our dimer models depicted in Fig. 1 then correspond to $\vec{N}$ pointing along positive or negative x,y,z directions, respectively. Finally, let $\vec{\phi}=(\phi_1,\phi_2)$ be a two-component vector combining the two complex fields ϕ_1 and ϕ_2.

We can now write the effective Ginzburg-Landau action as

$$\mathcal{S}_{\text{eff}} = \beta\int d^3r\big[|(\nabla - i\vec{\alpha})\vec{\phi}|^2 + U(\vec{N}) + \mathcal{L}(\vec{\alpha})\big],$$

(26)

where the first $|\ldots|^2$ term is a minimal coupling of the two complex fields to the dual $U(1)$ gauge field and $\mathcal{L}(\vec{\alpha})$ is the usual Maxwell's term for the gauge field. The potential $U(\vec{N})$ is determined by the underlying symmetries of the various dimer models, which are summarized in Table I. This potential therefore varies for the individual models as discussed in more detail below.

Note that the action (26) does not contain any time derivatives. The reason is that in the presence of such time-derivative terms and periodic boundary conditions in imaginary time, all modes with nonzero Matsubara frequencies are more massive than the zero-frequency mode of interest here and can be integrated out.

1. 1-GS model

The ground state of the 1-GS dimer model is a single columnar ordering pattern, which we choose to be oriented along the z direction. The effective Ginzburg-Landau action for this model is thus required to be invariant under the transformations T_x, T_y, and $R_{\pi/2,Rxy}$ only. In particular, the potential $U(\vec{N})$ in the action (26) has the general form

$$U(\vec{N}) = u_2|\vec{N}| + v_2 N_z = (u_2 + v_2)|\phi_1|^2 + (u_2 - v_2)|\phi_2|^2,$$
(27)

where we have only included terms up to quadratic order in the complex fields and introduced two coupling constants u_2 and v_2. Note that the potential $U(\vec{N})$ introduces two inequivalent mass terms for the two complex fields. As we reduce temperature, it will be the complex field with smaller mass that will condense, thereby leading to a condensation of the monopoles (while the other field still has vanishing expectation value). The corresponding phase transition can thus be described by a field theory with just one complex field coupled to a $U(1)$ gauge field which is known to be a *continuous* transition in the inverted 3D *XY* universality class.[21] At this Higgs transition, the system spontaneously breaks the $U(1)$ gauge symmetry, which leads to the characteristic confinement of charge excitations, e.g., the monomers in the language of the dimer model. We further note that at this transition, the system does not break any lattice symmetries.

To summarize our results for the 1-GS model, both our numerical simulations and field theory analysis come to the consistent and unambiguous conclusion that the transition between the Coulomb phase and a long-range ordered dimer crystal in this model is a continuous transition in the (inverted) 3D *XY* universality class. We again emphasize that such a continuous transition cannot be explained by the standard LGW paradigm.

2. 2-GS and 4-GS models

We now turn to the 2-GS and 4-GS models which we have seen to exhibit direct first-order thermal transitions. Although the two models have complementary ground-state manifolds, they are invariant under the exact same lattice transformations. As given in Table I, these are the three lattice translations T_x, T_y, and T_z as well as rotation around the z axis, $R_{\pi/2,Rxy}$. The symmetry-allowed potential terms up to quartic order in the Ginzburg-Landau action (26) are thus given by

$$U(\vec{N}) = u_2|\vec{N}| + u_4|\vec{N}|^2 + v_4 N_z^2.$$
(28)

For the 4-GS model $v_4 > 0$, so the N_z^2 term modulates $\vec{\phi}$ by the constraint $|\phi_1| = |\phi_2|$ and prefers the order parameter $\vec{N}$ to point in the xy plane. Noteworthily, this is still a continuously connected manifold with an internal $U(1)$ symmetry for the order parameter. Note that the system does not need to break any lattice symmetries to satisfy this constraint (in contrast to the 6-GS model which we will discuss in the next section). At the transition, when the complex fields $\vec{\phi}$ condense, the order parameter $\vec{N}$ becomes nonzero and points along one of the four lattice directions in the xy plane. Note

that at this Higgs transition, the system not only spontaneously breaks the $U(1)$ gauge symmetry, but *simultaneously* also the $U(1)$ order parameter symmetry as well as the fourfold lattice symmetry.

The action (28) exactly corresponds to the one studied for an easy-plane quantum antiferromagnet in the context of deconfined quantum criticality.[22,23] While analytical investigations of this action have suggested a continuous phase transition,[23] extensive numerical results have pointed to a weak first-order transition,[24,25] which is also what we find in our present numerical analysis.

For the 2-GS model, the order parameter $\vec{N}$ wants to point along the z direction, e.g., N_z becomes maximal, which implies (contrary to the 4-GS model) that $v_4 < 0$. This leaves the system with a disconnected manifold (of two points) for fixed magnitude $|\vec{N}|$ either preferring $|\phi_1| = 0$ or $|\phi_2| = 0$ and resulting in a Z_2 symmetry for the order parameter.

In contrast to the 1-GS model, this theory cannot be reduced to a field theory with just one complex field *without* breaking the lattice symmetry T_z. One possibility now is to have *two* subsequent transitions where we first break the lattice symmetry at a higher temperature and subsequently observe a Higgs transition at a lower temperature (with an exotic intermediate phase of coexisting Coulomb and dimer crystal correlations). In terms of the complex fields $\vec{\phi}$, the system would spontaneously select one of the two possibilities $|\phi_1| \neq 0, |\phi_2| = 0$ or $|\phi_1| = 0, |\phi_2| \neq 0$ at the first transition. At the second transition, the nonvanishing ϕ field would require a fixed phase in a Higgs transition.

Another possibility is to have one direct transition. However, it is hard to imagine a field theory giving rise to a continuous transition where the spontaneous breaking of the discrete Z_2 order parameter symmetry occurs simultaneously with the Higgs transition breaking the $U(1)$ gauge theory. Thus, we conclude that a *direct* transition is likely first order. The strongest support for this analytical scenario, of course, comes from our numerical simulations which unambiguously find a direct, first-order transition.

3. 6-GS model

Finally, we turn to the 6-GS model which respects all the cubic lattice symmetries. In writing down a symmetry-allowed potential for the action (26), we consider the simplest invariants of the form

$$U(\vec{N}) = V(|\vec{N}|) + v_8 I_8(\vec{N}),$$
(29)

where $I_8(\vec{N}) = N_x^2 N_y^2 + N_y^2 N_z^2 + N_x^2 N_z^2$ is an eighth order term in the complex fields $\vec{\phi}$ and we adopted a notation similar to the one of Ref. 19. Again we can expand the potential term $V(|\vec{N}|) = u_2|\vec{N}| + u_4|\vec{N}|^2 + \cdots$. Omitting the eighth order term in Eq. (29) gives an $SU(2)$ invariant action, which has attracted some interest due to recent proposals of $SU(2)$ invariant deconfined quantum critical points, as suggested in the $J-Q$ quantum model.[25–27]

Following the line of arguments in Ref. 19, the confining Higgs transition (which we observe) occurs for $u_2 < 0$ and $|\vec{N}|$ *simultaneously* acquires a finite magnitude, e.g., the $U(1)$ gauge symmetry and the lattice symmetry are broken at the

same transition. As argued in Ref. 19, one of the six columnar ground states is selected by the eighth order term $v_8 I_8(\vec{N})$, with $v_8 > 0$. Since the Higgs transition of the action (26) is suggested to be continuous without this eighth-order term and this term is likely irrelevant (due to its high order), we conclude that the action (29) allows for a continuous transition. This seems to be in agreement with the numerical evidence of Ref. 4 and our present numerical analysis interpolating between the 4-GS and 6-GS models.

The $SU(2)$ invariant action (29) without the eighth-order term has recently been discussed in terms of direct numerical simulations.[28,29] However, it has remained subtle to resolve the nature of the transition associated with this action and to differentiate a continuous transition[28] from a weakly first-order process.[29] How the nature of this transition potentially changes as one includes the eighth order term in the action (29) is an open question. However, direct numerical simulation of an action similar to Eq. (29) reported a continuous transition with exponents close but apparently different from those of the 3D XY model.[30]

4. Interpolated models

Finally, we briefly turn to the models interpolating between models exhibiting continuous and first-order transitions as discussed in Sec. III. Interpolating between the 1-GS and 2-GS models, the system exhibits for all interpolation parameters $0 \leq \lambda < 1$ the same lattice symmetries and is therefore described by the same Ginzburg-Landau action with potential (27) as the 1-GS model. This symmetry analysis suggests that for all $\lambda < 1$, the two complex fields ϕ_1, ϕ_2 acquire different masses and we can describe the action in terms of a *single* complex field coupled to a $U(1)$ gauge field. On the other hand, we expect the strong first-order transition of the 2-GS model ($\lambda = 1$) to be stable toward small perturbations and therefore to extend over a finite region $\lambda < 1$. As a consequence, there should be a multicritical point λ_c where the line of continuous transitions for $\lambda \leq \lambda_c$ meets the first-order line for $\lambda > \lambda_c$.

Interpolating between the 4-GS and 6-GS models, the system exhibits for all interpolation parameters $0 \leq \lambda < 1$ the same lattice symmetries, while the symmetries change for the end point $\lambda = 1$ which corresponds to the 6-GS model (see also Table I). Again, this symmetry analysis suggests that all interpolated models with $0 \leq \lambda < 1$ are described by the same Ginzburg-Landau action with potential (28). This seems to be in agreement with our numerical results suggesting that all models with $0 \leq \lambda < 1$ exhibit first-order transitions.

V. INTERMEDIATE PARAMAGNET

Finally, we turn to a second family of dimer models that also energetically favor specific subsets of the six columnar ordering patterns illustrated in Fig. 1. The distinct feature of this second family of dimer models is that they harbor *two consecutive* thermal phase transitions. The high-temperature phase transition out of the Coulomb phase is again driven by the condensation of monopoles with confining monomer excitations. However, this phase transition is into a paramagnetic phase without dimer crystalline order which only forms

at the low-temperature transition. Thus, we are left with an unusual sequence of phases in these models with the paramagnet residing at *intermediate* temperature scales.

A. Second family of dimer models

Our second family of dimer models explores other combinations of the six columnar ordering patterns in Fig. 1 as ground states. The common characteristic in selecting the admissible ground states is that for at least one lattice direction, we choose only one of the two possible columnar orderings and there is more than one ground state. If we name the models by the lattice directions for which ground states are chosen, these are the xy, xyz, xxy, $xyzz$, and $xxyyz$ models. In this nomenclature, the models in our first family of models would be named z, zz, $xxyy$, and $xxyyzz$ for the 1-GS, 2-GS, 4-GS, and 6-GS model, respectively.

We will not discuss all possible models in this section, but concentrate on the xy model with Hamiltonian

$$\mathcal{H}_{xy} = -\sum_{\square} (n_=^e + n_{//}^e), \tag{30}$$

where we have chosen the columnar dimer orderings on the even bonds in the x and y lattice directions as ground states.

We summarize our numerical results for this model in Fig. 15. The two consecutive thermal transitions both carry distinct thermodynamic signatures with a double-peak structure emerging in the specific heat. At the high-temperature transition out of the Coulomb phase, the monomer confinement length drops again indicating that this transition is due to monopole condensation. A finite-size scaling analysis reveals a distinct crossing point (see Fig. 16) indicating a continuous transition into the intermediate-temperature paramagnet.

We argue that this transition is again described by the inverted 3D XY universality class. We first notice that the temperature of the Coulomb transition in the xy model ($T_c \simeq 2.247$) turns out to be close to the one found for the 1-GS model (where $T_c \simeq 2.276$). Another indicator that the Coulomb transitions in these two models are closely related and probably of the same universality class is that the universal value of the confinement length at the crossing point is $\tilde{\xi}(T_c) \approx 0.920 \pm 0.001$, which is rather close to the one found for the 1-GS model [$\tilde{\xi}(T_c) \approx 0.923 \pm 0.001$]. As a final argument, we find an excellent data collapse of the confining length measured in the vicinity of this transition for different system sizes when rescaling the data with the correlation length exponent $\nu = 0.6717$ of the 3D XY universality class (see Fig. 17).

At the low-temperature transition, the system spontaneously selects one of the two possible columnar ordering

specific heat

(a)

energy

(b)

confinement length

(c)
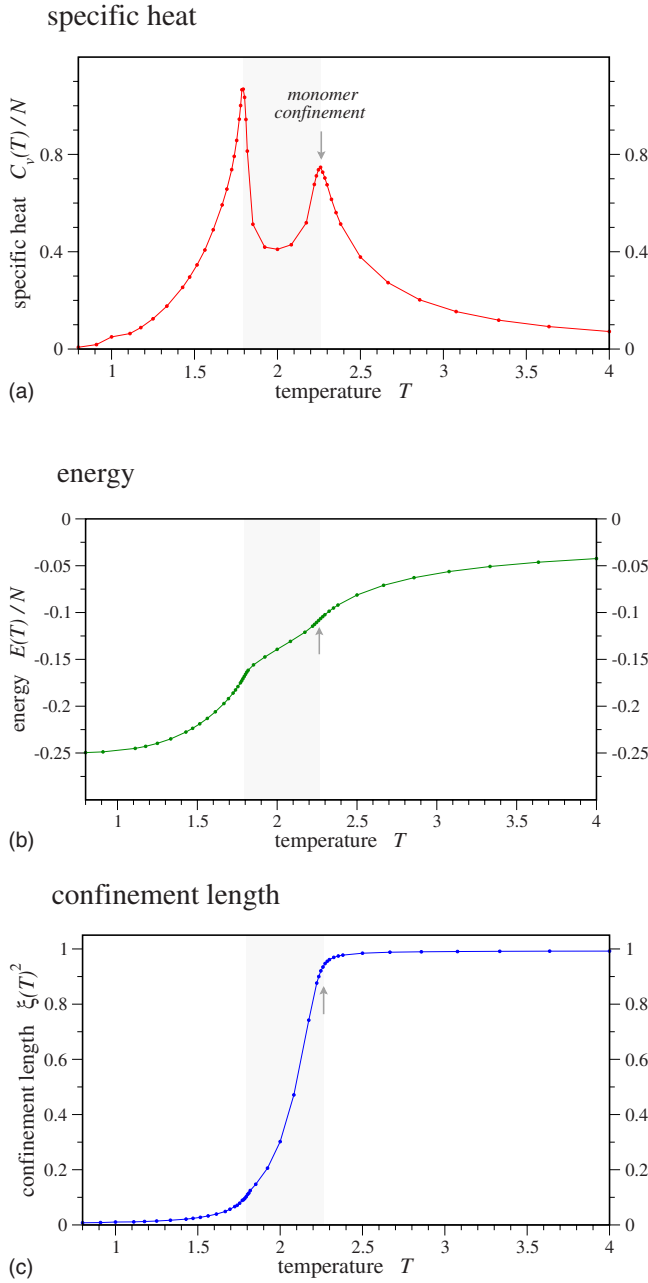
FIG. 15. (Color online) Overview of the *xy* model that favors one columnar ordering pattern along the *x* and *y* lattice directions: (a) specific heat per site $C_v(T)/N$, (b) energy per site $E(T)/N$, and (c) confinement length $\xi(T)^2$. This model undergoes an unusual sequence of phases with a paramagnetic phase (shaded area) at intermediate temperature scales. The high-temperature transition out of the Coulomb phase (denoted by an arrow) is a monomer confinement transition, while the dimer crystal forms only at the low-temperature phase transition.

patterns and we observe a sudden increase of the number of plaquettes with parallel dimers, e.g., $n_=^e$ or $n_{//}^e$, respectively (see Fig. 18). The sharp jump of this order parameter indicates a first-order phase transition, which is confirmed by the bimodal structure of energy histograms close to this transition point (see Fig. 19).
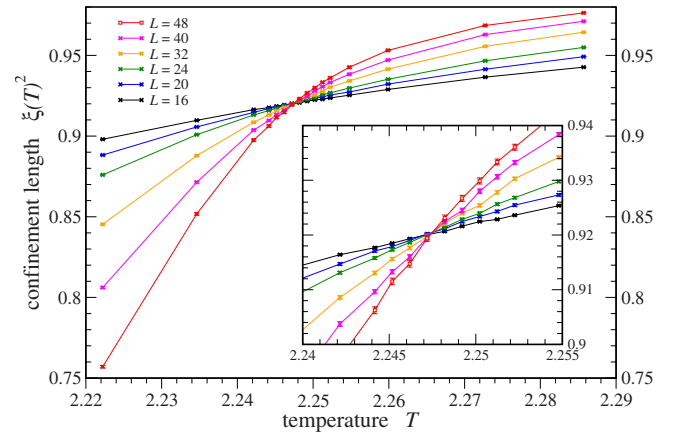
FIG. 16. (Color online) Crossing point of the confinement length $\xi^2(T)$ for different system sizes at the high-temperature phase transition out of the Coulomb phase for the *xy* model.

B. Theoretical Analysis

We can discuss the nature of the phase transitions for this second type of dimer models by again analyzing the symmetry-allowed effective Ginzburg-Landau actions in full analogy to the discussion in Sec. IV B for the first family of dimer models. With the lattice symmetries for the individual members of this second family of dimer models given in Table I, we find the following potentials for the Ginzburg-Landau action in Eq. (26):

$$U(\vec{N}) = \begin{cases} u_2|\vec{N}| + v_2(N_x + N_y), & xy \text{ model} \\ u_2|\vec{N}| + v_2 N_y, & xxy \text{ model} \\ u_2|\vec{N}| + v_2(N_x + N_y + N_z), & xyz \text{ model} \\ u_2|\vec{N}| + v_2(N_x + N_y), & xyzz \text{ model} \\ u_2|\vec{N}| + v_2 N_z, & xxyyz \text{ model}. \end{cases}$$

(31)

For all models, we can diagonalize the quadratic part in these potentials by performing an $SU(2)$ rotation in the (ϕ_1, ϕ_2) space such that the potentials (31) take an identical
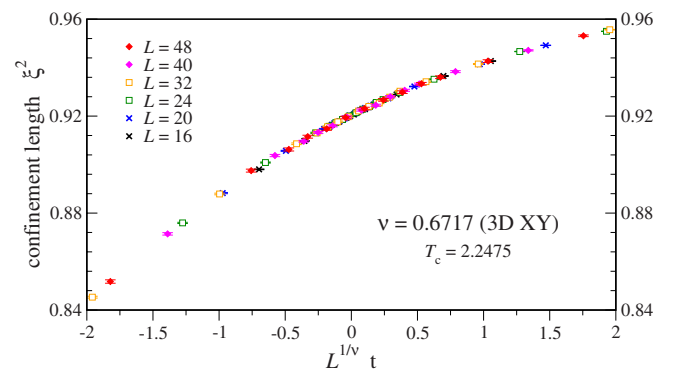
FIG. 17. (Color online) Data collapse for the confinement length ξ^2 as a function of $L^{1/\nu}t$, where $t=(T-T_c)/T_c$, with $T_c=2.2475$. The critical exponent $\nu=0.6717$ corresponds to the 3D *XY* universality class.
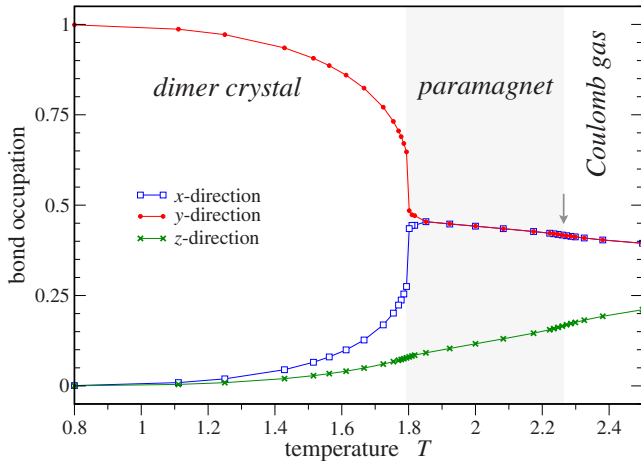
FIG. 18. (Color online) Bond occupation along the x, y, and z lattice directions vs temperature for the xy model. At low temperatures, data are shown for a system that spontaneously orders along the y direction (other systems spontaneously order along the x direction). The low-temperature transition between the paramagnet and the dimer crystal is accompanied by a sudden increase of the bond occupation along the preferred lattice direction. The high-temperature transition between the Coulomb gas and the paramagnet where the monomers confine is indicated by the arrow.

form as given in Eq. (27) for the 1-GS model. As a consequence, we expect the high-temperature transition out of the Coulomb phase in all these models to be described by the same Higgs mechanism we identified for the 1-GS model resulting in a continuous transition in the inverted 3D *XY* universality class. Our numerics give supporting evidence for a continuous transition in this universality class as discussed above.

The main distinction between the models in our second family of models and those in the first set of models is that here we can break an additional lattice symmetry which apparently gives rise to the second transition into the dimer crystal phase at lower temperatures. We argue that this second low-temperature phase transition is generically a first-
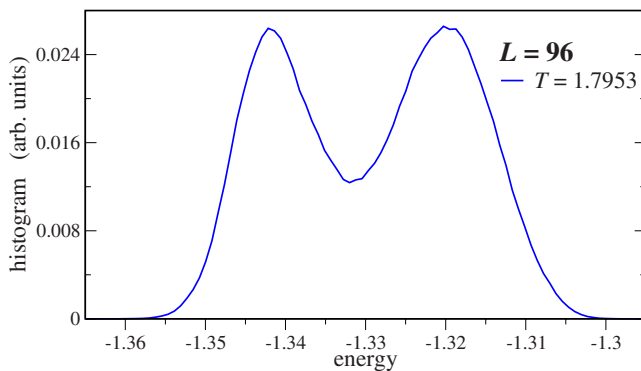
FIG. 19. (Color online) Energy histogram in the vicinity of the low-temperature phase transition, which we argue to be a thermal analog of a spin-flop transition (see text). Our numerics indicate a weak first-order transition by a double-peak structure in the energy histogram, which emerges for larger system sizes. Here, system size is $L=96$.

order transition analog to a *spin-flop* transition. To see this analogy, consider the xy model with the potential $U(\vec{N}) = u_2|\vec{N}| + v_2(N_x + N_y)$ in the Ginzburg-Landau action. Below the confinement transition, the order parameter $\vec{N}$ has a non-zero expectation value (since the monopoles are condensed), but points half-way between the x and y directions, thereby minimizing the second term in the potential. This is also evident in our numerical simulations as shown in Fig. 18. At very low temperature, however, we know that the system must (because there will be no dimer fluctuations) spontaneously order along one of the two lattice directions, thus breaking the symmetry between x and y directions. Therefore, the spin $\vec{N}$ must reorient away from the (110) axis to the (100) or (010) axis. To describe this, we require additional higher-order terms in the potential $U(\vec{N})$ of the form $N_x N_y$, $N_x^2 N_y^2$, etc. At low temperature, since the magnitude of the spin becomes large ($|N|=1$ as there are no fluctuations), such terms are no longer negligible. On lowering the temperature and increasing these higher order terms, we expect the minimum directions of this energy function to abruptly switch to their low-temperature values. This is indeed the most commonly occurring situation in spin systems, in which such a first-order reorientation is known as a "spin-flop" transition. This expectation, arrived at above from "analytical" field theory considerations, is indeed verified in the numerics (see Fig. 19).

VI. DISCUSSION

Recent years have seen an extensive search for continuous phase transitions beyond the LGW paradigm, which were originally suggested to occur in certain quantum models.[22,23] In this paper, we have demonstrated that this exotic physics can manifest itself also in various *classical* models. This, of course, is not much of a surprise since the universality of continuous phase transitions mandates that they occur in a large variety of models, including classical ones. Nevertheless, it is amusing to note that such unconventional phase transitions and the sophisticated ordering mechanisms associated with them can actually be found in simple variations of one of the golden models of statistical mechanics, namely, the dimer model. The key ingredient giving rise to this exotic physics is a constraint which enforces close-packed coverings of hard-core dimers. In a way, this readily builds into the classical model a certain level of frustration which is often invoked to be a key ingredient for quantum models to exhibit non-LGW criticality.

Besides the important step to directly establish the occurrence of non-LGW transitions in these dimer models, we view several advantages arising from their classical nature. (i) Classical models are notoriously simpler to analyze, both theoretically and numerically, than quantum models. They are accessible to Monte Carlo approaches, thus allowing to study critical phenomena through the direct simulation of large systems. For the specific dimer models at hand, the existence of a highly efficient Monte Carlo worm algorithm is also very attractive. (ii) These models ease the identification of the necessary ingredients that are needed to cause

non-LGW physics in a lattice model (such as lattice and/or continuous symmetries). This further opens the possibility of "reverse engineering" or "rolling back the path integral" to obtain two-dimensional quantum models that exhibit the same non-LGW criticality as their three-dimensional classical counterparts. Such a classical-to-quantum mapping was recently used in Ref. 31. (iii) The stability of certain critical behavior can be easily explored in variations of these classical models, e.g., through the inclusion of perturbations or by extrapolating terms (as performed in the current study). For instance, a yet-to-be-explored possibility is to include terms that *frustrate* the columnar ordering. A similar situation in a quantum model would generically come with a sign problem in quantum Monte Carlo simulations, putting serious limitations to any numerical study. (iv) Finally, the sheer simplicity of these models might indicate that non-LGW transitions are not that exotic after all.

[1] D. L. Bergman, R. Shindou, G. A. Fiete, and L. Balents, Phys. Rev. Lett. **96**, 097207 (2006).

[2] D. Bergman, J. Alicea, E. Gull, S. Trebst, and L. Balents, Nat. Phys. **3**, 487 (2007).

[3] D. L. Bergman, G. A. Fiete, and L. Balents, Phys. Rev. B **73**, 134402 (2006).

[4] F. Alet, G. Misguich, V. Pasquier, R. Moessner, and J. L. Jacobsen, Phys. Rev. Lett. **97**, 030403 (2006).

[5] T. S. Pickles, T. E. Saunders, and J. T. Chalker, EPL **84**, 36002 (2008).

[6] C. Castelnovo, C. Chamon, C. Mudry, and P. Pujol, Phys. Rev. B **73**, 144411 (2006).

[7] D. A. Huse, W. Krauth, R. Moessner, and S. L. Sondhi, Phys. Rev. Lett. **91**, 167004 (2003).

[8] M. Hermele, M. P. A. Fisher, and L. Balents, Phys. Rev. B **69**, 064404 (2004).

[9] S. V. Isakov, K. Gregor, R. Moessner, and S. L. Sondhi, Phys. Rev. Lett. **93**, 167204 (2004); C. L. Henley, Phys. Rev. B **71**, 014424 (2005).

[10] F. H. Stillinger and M. A. Cotter, J. Chem. Phys. **58**, 2532 (1973).

[11] J. Villain and J. Schneider, in *Physics and Chemistry of Ice*, edited by E. Whalley, S. J. Jones, and L. W. Gold (Royal Society of Canada, Ottawa, 1973); see also J. Villain, Solid State Commun. **10**, 967 (1972).

[12] R. W. Youngblood and J. D. Axe, Phys. Rev. B **23**, 232 (1981).

[13] G. Misguich, V. Pasquier, and F. Alet, Phys. Rev. B **78**, 100402(R) (2008).

[14] A. W. Sandvik and R. Moessner, Phys. Rev. B **73**, 144504 (2006).

[15] F. Alet, Y. Ikhlef, J. L. Jacobsen, G. Misguich, and V. Pasquier, Phys. Rev. E **74**, 041124 (2006).

[16] M. Campostrini, M. Hasenbusch, A. Pelissetto, and E. Vicari, Phys. Rev. B **74**, 144506 (2006).

[17] A. Cucchieri *et al.*, J. Phys. A **35**, 6517 (2002).

[18] A similar value $\tilde{\xi}^2(T_c)=0.9204(10)$ is found for the 3D isotropic link-current model [see for instance F. Alet and E. Sørensen, Phys. Rev. E **67**, 015701 (2003)] which has a phase transition in the 3D XY universality class [F. Alet (unpublished)]. The comparison to the current study needs a further investigation of the role of anisotropy in the link-current model (as the dimer models are themselves anisotropic).

[19] O. I. Motrunich and T. Senthil, Phys. Rev. B **71**, 125102 (2005).

[20] J. B. Kogut, Rev. Mod. Phys. **51**, 659 (1979).

[21] C. Dasgupta and B. I. Halperin, Phys. Rev. Lett. **47**, 1556 (1981).

[22] T. Senthil, A. Vishwanath, L. Balents, S. Sachdev, and M. P. A. Fisher, Science **303**, 1490 (2004).

[23] T. Senthil, L. Balents, S. Sachdev, A. Vishwanath, and M. P. A. Fisher, Phys. Rev. B **70**, 144407 (2004).

[24] S. Kragset, E. Smørgrav, J. Hove, F. S. Nogueira, and A. Sudbø, Phys. Rev. Lett. **97**, 247201 (2006).

[25] F. J. Jiang, M. Nyfeler, S. Chandrasekharan, and U. J. Wiese, J. Stat. Mech.: Theory Exp. (2008) P02009.

[26] A. W. Sandvik, Phys. Rev. Lett. **98**, 227202 (2007).

[27] R. G. Melko and R. K. Kaul, Phys. Rev. Lett. **100**, 017203 (2008).

[28] O. I. Motrunich and A. Vishwanath, arXiv:0805.1494 (unpublished).

[29] A. B. Kuklov, M. Matsumoto, N. V. Prokof'ev, B. V. Svistunov, and M. Troyer, Phys. Rev. Lett. **101**, 050405 (2008).

[30] D. Charrier, F. Alet, and P. Pujol, Phys. Rev. Lett. **101**, 167205 (2008).

[31] S. Powell and J. T. Chalker, Phys. Rev. Lett. **101**, 155702 (2008); Phys. Rev. B **78**, 024422 (2008).

[32] A. F. Albuquerque *et al.*, J. Magn. Magn. Mater. **310**, 1187 (2007).

[33] M. Troyer, B. Ammon, and E. Heeb, Lect. Notes Comput. Sci. **1505**, 191 (1998).

[34] The only difference with the algorithms presented in Refs. 14 and 15 concerns the computation of the weights w_{ij} [see, for instance, in, e.g., Eq. (33) of Ref. 15 and the related heat-bath probabilities] which depend on the energetics of the model simulated.